Unveiling diurnal aerosol layer height variability from space using deep learning

Yulong Fan [a], Lin Sun [a,**], Zhihui Wang [b], Shulin Pang [c], Jing Wei [d,e,*]

[a] College of Geodesy and Geomatics, Shandong University of Science and Technology, Qingdao, China
[b] Anhui Institute of Optics and Fine Mechanics, Hefei Institutes of Physical Science, Chinese Academy of Sciences, Hefei, China
[c] Innovation Research Center of Satellite Application, Faculty of Geographical Science, Beijing Normal University, Beijing, China
[d] MEEKL-AERM, College of Environmental Sciences and Engineering, Institute of Tibetan Plateau, and Center for Environment and Health, Peking University, Beijing, China
[e] Department of Atmospheric and Oceanic Science, Earth System Science Interdisciplinary Center, University of Maryland, College Park, MD, USA

ARTICLE INFO

ABSTRACT

The vertical distribution of aerosols is crucial for extensive climate and environment studies but is severely constrained by the limited availability of ground-based observations and the low spatiotemporal resolutions of Lidar satellite measurements. Multi-spectral passive satellites offer the potential to address these gaps by providing large-scale, high-temporal-resolution observations, making them a promising tool for enhancing current aerosol vertical distribution data. However, traditional methods, which rely heavily on physical assumptions and prior knowledge, often struggle to deliver robust and accurate aerosol vertical profiles. Thus, we develop a novel retrieval framework that combines two advanced deep-learning models, locally-feature-focused Transformer and globally-feature-focused Fully Connected Neural Network (FCNN), referred to as TF-FCNN, to estimate hourly aerosol distributions at different heights (i.e., 0.01–1 km, 1–2 km, and 2–3 km) with 2-km spatial resolution, using multi-source satellite data, including Cloud-Aerosol Lidar and Infrared Pathfinder Satellite Observations (CALIPSO), Himawari-8 and Moderate Resolution Imaging Spectroradiometer (MODIS). This hybrid framework is thoroughly analyzed using an eXplainable Artificial Intelligence (XAI)-based SHapley Additive exPlanations (SHAP) approach, which reveals that shortwave bands and brightness temperature are the most influential features, contributing approximately 63 % to the model predictions. Validation results demonstrate that the model provides reliable hourly aerosol vertical distributions across different heights in Australia, achieving high overall sample-based cross-validation coefficients of determination (CV-R^2) ranging from 0.81 to 0.90 (average = 0.88). Our hourly retrievals indicate higher aerosol loadings at lower altitudes (0.01–1 km) than higher ones (1–2 km and 2–3 km) in most areas, likely due to significant anthropogenic and natural emissions from the ground. Furthermore, we observe substantial increases in aerosol concentrations over time and enhanced diurnal variations across altitudes during highly polluted cases, including urban haze and wildfires. These unique insights into the spatial distribution of aerosol vertical layers are crucial for effective air pollution control and management.

1. Introduction

Atmospheric aerosols can absorb and scatter solar radiation at different wavelengths, which is important for the global radiation balance and climate change (Lee et al., 2023). Also, aerosols rooted in toxic metals, organic chemicals, and microorganisms can damage the atmospheric environment and pose significant health risks (Feng et al., 2024; Shiraiwa et al., 2017). Unlike other atmospheric components, such as greenhouse gases, aerosols have a localized impact on climate and environment, exhibiting strong spatial heterogeneities and temporal variabilities (Jiang et al., 2023). In addition to horizontal distribution, aerosols also have significant spatiotemporal variations in the vertical

---

direction, especially under conditions with complex sources and rapid transmission, such as urban haze and wildfires (Heinold et al., 2022; Sun et al., 2018). Therefore, timely obtaining precise aerosol distribution information is crucial for mitigating their climatic, ecological, and health effects.

However, accurately quantifying aerosol vertical distributions with sufficient spatial coverage remains a significant challenge. Traditional approaches for retrieving aerosol vertical distributions primarily rely on ground-based remote sensing using lidar, such as MPLNET (Micro-Pulse Lidar Network) (Campbell et al., 2002; Wang et al., 2020) and EAR-LINET (European Aerosol Research Lidar Network) (Pappalardo et al., 2014), active space-based lidar like CALIPSO (Cloud-Aerosol Lidar and Infrared Pathfinder Satellite Observations) (Kim et al., 2018; Kudo et al., 2023), and passive satellite measurements combined with radiative transfer modeling (Chen et al., 2021; Lemmouchi et al., 2022; Maheshwarkar et al., 2024; Sanders et al., 2015; Sanghavi et al., 2012; Xu et al., 2019). While these methods provide valuable vertical aerosol information, they suffer from several limitations. Ground-based lidar networks offer only localized observations and are restricted to clear-sky conditions (Gupta et al., 2021; He et al., 2008). CALIPSO plays an essential role in studying long-term global aerosol vertical distributions, as it has provided more than a decade of global observations since 2011. However, its low temporal resolution of ~ 16 days makes it difficult to capture short-term variations in rapidly changing aerosols. In addition, it has a coarse horizontal spatial resolution (17.6 km in longitude and 5.6 km in latitude) due to its point-shape observation mode and line-shape track, limiting its ability to capture significant aerosol variations at medium or small (urban) scales (Adams et al., 2012; Huang et al., 2015). Passive satellite retrievals depend on complex inverse modeling, which is highly sensitive to empirical assumptions, prior knowledge, and surface reflectance conditions (Maheshwarkar et al., 2024; Xu et al., 2017). These approaches are also computationally intensive due to their iterative nature, making them less suitable for large-scale applications (Choi et al., 2019; Kudo et al., 2023).

Recently, machine learning (ML) has become increasingly popular for its strong data mining capabilities and has been applied in a handful of studies to retrieve aerosol vertical distributions. Chen et al. (2022) employed the Extra Trees model, using CALIPSO AOD and auxiliary data, to estimate the vertical distribution of $PM_{2.5}$ at a 16-day resolution in East China. Pashayi et al. (2025) adopted the XGBoost model to estimate instantaneous AOD at four atmospheric layers (1.5, 3, 5, and 10 km) over Europe, using CALIPSO profiles and SEVIRI (Spinning Enhanced Visible and Infrared Imager) data. Li et al. (2025) developed an XGBoost-LightGBM-Wavelet (XLW) model to derive an annual three-dimensional aerosol extinction coefficient dataset at 167 layers from multiple data sources across China. Wang et al. (2025) combined the long short-term memory (LSTM) and Transformer models to estimate aerosol layer height at a 16-day resolution from the OCO-2 (Orbiting Carbon Observatory-2) hyperspectral observations in West Africa. However, the application of ML to aerosol vertical distribution retrieval remains in its early stages, with most studies relying on traditional tree-based models. These models exhibit limited capability to capture intricate spatial–temporal dependencies when retrieving weak aerosol vertical distributions from satellite observations. In contrast, our model effectively captures spatiotemporal correlations and models complex nonlinear relationships by extracting fine-scale local features. Furthermore, existing products suffer from limited accuracy and, more importantly, typically provide coarse temporal resolutions, often daily or multi-day (e.g., 16-day or annual) averages, limiting their ability to capture diurnal variability in aerosol distribution, which is especially important in local areas (like urban) with highly dynamic emission sources.

To overcome the limitations of traditional methods (e.g., optimal estimation), we develop a novel deep learning framework (TF-FCNN) that integrates a Transformer and a Fully Connected Neural Network to retrieve high-spatial-resolution, hourly aerosol vertical profiles from

Himawari-8 satellite observations. This hybrid model leverages their complementary strengths: the Transformer excels at capturing long-range dependencies (relationships or correlations between data points that are far apart in space or time) and spatiotemporal correlations, while the FCNN effectively models complex nonlinear relationships and extracts fine-scale local features through its strong nonlinear fitting capability. By combining global and local information from multi-source datasets and incorporating crucial physical parameters, particularly bidirectional reflectance distribution function (BRDF) factors, the framework significantly enhances both the accuracy and spatial completeness of aerosol profile retrievals. Finally, the fidelity of our model is demonstrated through comprehensive validation approaches and analysis of aerosol vertical distribution patterns across Australia, including their diurnal variations under urban haze and wildfire conditions.

2. Data and materials

In this study, we selected Australia as the primary analysis region because it provides a relatively clean background with episodic yet significant aerosol events from both natural (wildfires) and anthropogenic (urban haze) sources, offering diverse but manageable test cases. Moreover, Australia's relatively simple aerosol environment allows us to access the fundamental feasibility and performance of our framework without the confounding influence of highly mixed aerosol sources.

2.1. CALIPSO measurements

CALIPSO Level 2 Aerosol Profile, Version 4–51 data product (CAL_-LID_L2_05kmAPro-Standard-V4-20) (Nasa/Larc/Sd/Asdc, 2018) for the year 2022 is used to provide aerosol vertical information as the ground truth for the ML modeling. This profile product is reported at a uniform spatial resolution of 0.06 km vertically and 5 km to 17.6 km horizontally over a nominal altitude range from 30 km to −0.5 km. Due to the on-board data averaging scheme, the vertical resolution of the aerosol profile data varies with altitude. In the tropospheric region (20 km to −0.5 km), the resolution is 0.06 km vertically, while in the stratospheric region (above 20 km), the vertical resolution is 0.18 km (Table S1). It is retrieved based on the attenuated backscatter signal observed by the CALIPSO at green (532 nm) and near-infrared (1064 nm) wavelengths. The calibration accuracy of CALIPSO attenuated backscatter coefficients at 532 nm is 1.0 % ± 3.5 %, as validated against NASA's airborne High Spectral Resolution Lidar (HSRL) measurements (Getzewich et al., 2018). The validation accuracy of CALIPSO AOD data is −5.1 % ± 8.5 % compared to Aerosol Robotic Network (AERONET) ground-based measurements (Kim et al., 2018). Despite the good calibration and validation accuracy, the remaining uncertainties suggest the inherent limitations of using CALIPSO as a reference and represent an upper bound on the achievable accuracy under real-world conditions when interpreting model evaluation results.

In this study, we divide the heights into three groups, including 0.01–1 km, 1–2 km, and 2–3 km, to reflect typical vertical distributions of aerosol layers observed over the study region and to facilitate clearer layer-by-layer analysis. The 3 km limit represents the typical vertical extent of aerosols in the lower troposphere, where most aerosol loading and relevant atmospheric processes occur. Capturing key variations within this range is highly relevant to surface air quality and regional climate impacts. These ranges roughly correspond to the surface layer, boundary layer, and lower free troposphere, which often exhibit distinct aerosol characteristics and transport mechanisms. For example, aerosols in the low layer (0.01–1 km) reflect near-surface aerosol emissions and deposition, while the boundary (1–2 km) layer captures the vertical diffusion and transport of aerosols (Liao et al., 2021; Vinjamuri et al., 2020). Aerosols at higher altitudes (> 2 km) typically exhibit low concentrations and remain stable, except during extreme events such as haze or wildfires that involve significant particulate emissions (Liao

et al., 2021). Additionally, binning the data into broader height intervals helps reduce the impact of vertical uncertainty and retrieval noise inherent in CALIPSO observations, particularly in weakly attenuating layers (Yu et al., 2010), thereby improving the robustness of the modeling. To ensure the sampling quality, the unreasonable values (< 0) from the product are eliminated before use, and only locations with valid retrievals at every vertical layer between 0 and 1 km are used to generate training labels and for validation purposes. Fig. S1 illustrates the spatial distribution of CALIPSO sampling counts corresponding to the validation points. The large number of missing values in the CALIPSO dataset is primarily due to signal attenuation caused by thick clouds, which prevent the lidar from detecting lower atmospheric layers. Additionally, increased solar background radiation during daytime and high surface reflectance over bright surfaces can reduce the signal-to-noise ratio and degrade signal quality (Kim et al., 2018; Mao et al., 2022; Tackett et al., 2023).

2.2. Himawari-8 observations

Himawari-8 L1 full-disk data, with multiple bands ranging from 0.47 μm to 13.3 μm and a high temporal resolution of 10 min (144 observations per day), is used as input for retrieving aerosol vertical distributions. Specifically, the top-of-atmosphere (TOA) reflectance from the first six shorted channels from 0.47 μm to 1.6 μm, serves as the primary input, and the brightness temperature (BT) at 11.2 μm is also included due to its high sensitivity to coarse aerosols like dust and smoke (Liu et al., 2024). In the full-disk observation mode, these data are initially acquired for a large region (approximately a quarter of the Earth: 60S–60 N; 80E–160 W), including eastern Asia and Australia, with various resolutions from 0.5 km to 2 km across bands. Therefore, the

spatial resolutions of the Himawari-8 observation at different bands are resampled to a consistent 2 km using the bidirectional linear interpolation method (Wei et al., 2023). Additionally, observation geometry, including satellite viewing zenith angle (VZ), solar zenith angle (SZ), and relative azimuth angle (RA), is incorporated to account for the effect of the light transmission path on the satellite signal. A series of spectral tests were conducted to filter out unsuitable retrieval pixels under cloud cover or over snow/ice and water surfaces, as detailed in Table S2.

2.3. MODIS product

The MCD19A3D (Collection 6.1) product at a high spatial resolution of 1 km is also employed to characterize the ground surface when retrieving aerosol vertical distributions. This dataset is derived from MODIS (Moderate Resolution Imaging Spectroradiometer) observations using the Multi-Angle Implementation of Atmospheric Correction (MAIAC) algorithm (Lyapustin et al., 2018). It provides three coefficients, isotropic (ISO), volumetric (VOL), and geometric (GEO), of the RossThick/Li-Sparse (RTLS) BRDF model for eight bands ranging from 0.47 μm to 2.11 μm, effectively characterizing the anisotropic reflectance properties of ground targets. Here, BRDF coefficients at three short-wavelength channels, including red (0.65 μm), green (0.55 μm), and blue (0.47 μm), which are more sensitive to aerosol properties and provide a favorable signal-to-noise ratio for aerosol detection compared to other spectral bands, are selected as inputs for our model. In this study, we utilize monthly BRDF data synthesized from the MCD19A3D daily products in our modeling. To minimize the effects of spatial gaps caused by cloud contamination, any remaining missing monthly values are further filled using seasonal averages, given the relatively small temporal variability. Additionally, the MOD14A1 Thermal Anomalies/
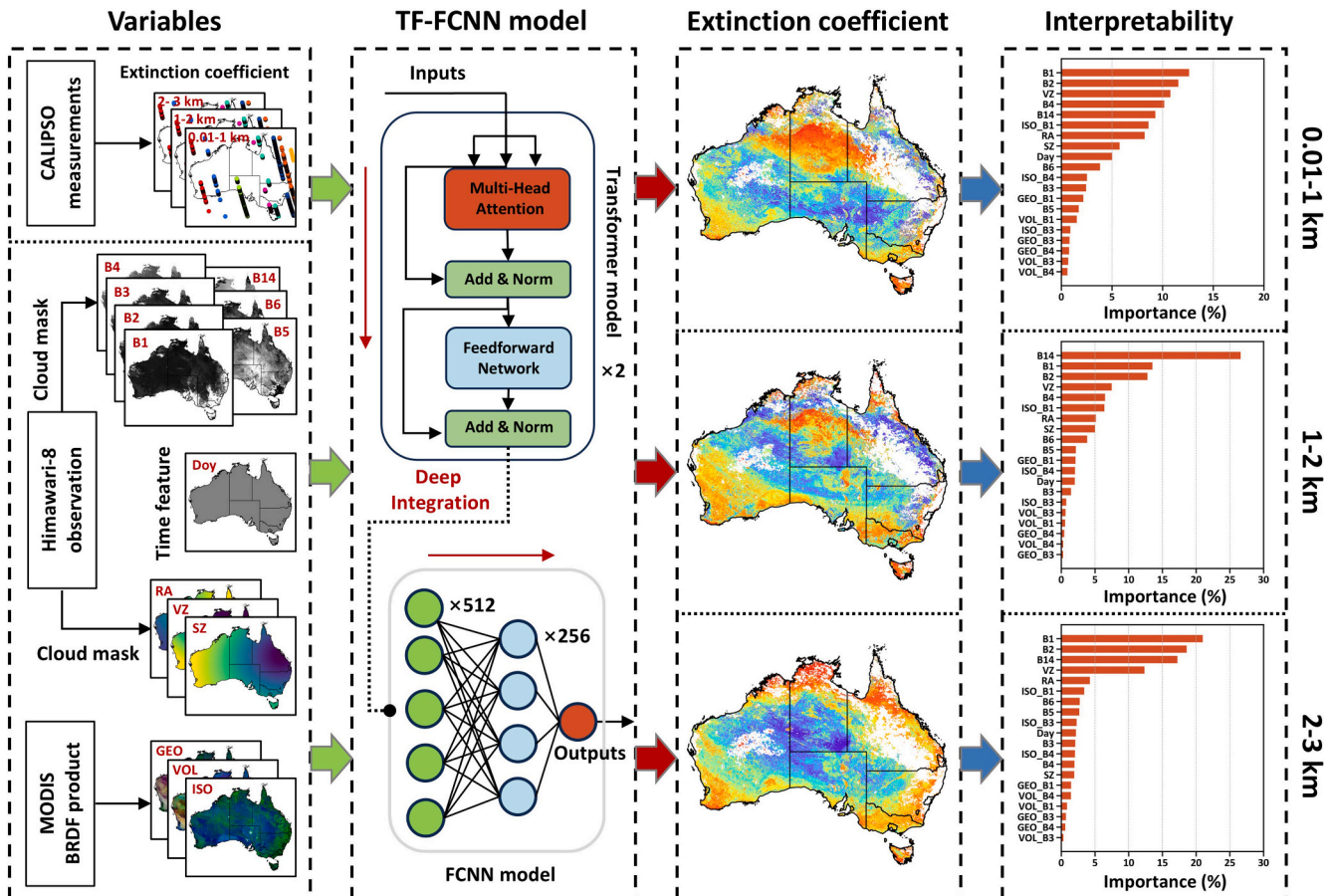

Fig. 1. Workflow for retrieving hourly aerosol vertical distributions from satellite observations using the developed hybrid deep learning model.

Fire (daily, 1 km) and MCD12Q1 Land Cover (yearly, 500 m) products are also collected to indicate the areas with wildfires and with different land-use types, respectively.

3. Aerosol vertical distribution retrieval framework

In this study, we developed an hourly aerosol vertical distribution retrieval framework, a novel hybrid deep-learning model, by combining active CALIPSO observations and passive Himawari-8 and MODIS imagery (Fig. 1). Within the framework, eXplainable Artificial Intelligence (XAI) technique is employed to enhance the interpretability and reveal the physical connections by quantifying the contributions of different variables on the model's outputs at various heights (i.e., 0.01–1 km, 1–2 km, and 2–3 km).

3.1. Feasibility analysis

The feasibility of retrieving aerosol vertical distributions using Himawari-8 imagery was first analyzed from a physical perspective using the Second Simulation of a Satellite Signal in the Solar Spectrum (6S) radiative transfer model. The 6S model simulates solar radiation captured by multi-spectral satellites from visible to near-infrared bands (0.25–4 μm) under varying observation geometries, atmospheric conditions, and aerosol models (Kotchenova et al., 2008). To evaluate the influence of aerosol vertical distributions on satellite signals, we defined four idealized profiles: H1 (all aerosols at a base height H), H2 (one-third at H, two-thirds at H + 0.24 km), H3 (half at H, half at H + 0.24 km), and H4 (two-thirds at H, one-third at H + 0.24 km). The vertical offset of + 0.24 km was selected to reflect small shifts in aerosol layer height
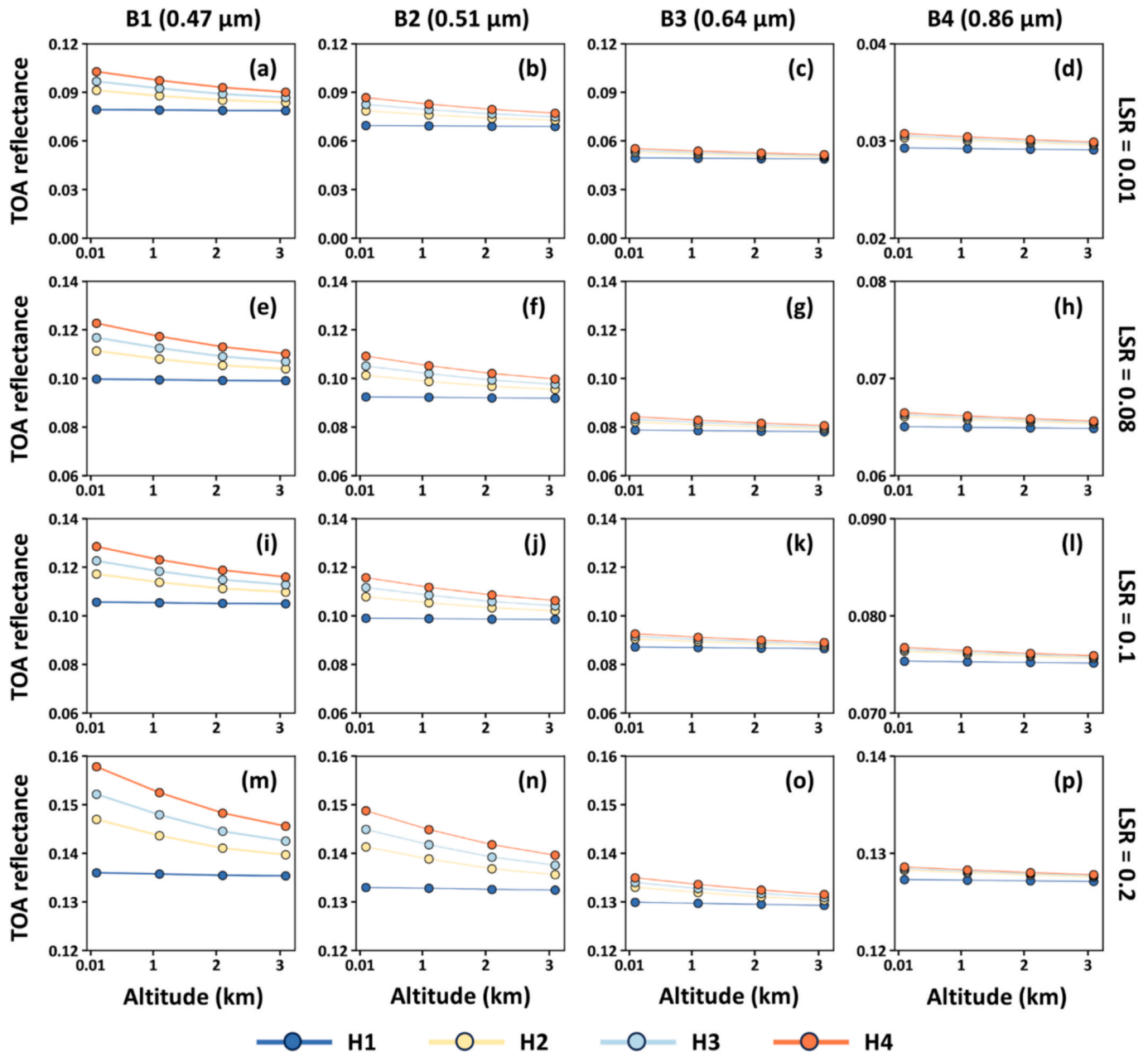

Fig. 2. Atmospheric radiative transfer simulations for Himawari-8 multi-spectral bands (B1-B4) under different aerosol vertical profiles, including H1 (all aerosols at a base height H), H2 (one-third at H, two-thirds at H + 0.24 km), H3 (half at H, half at H + 0.24 km), and H4 (two-thirds at H, one-third at H + 0.24 km). Simulations were conducted with fixed parameter settings (AOD = 0.9, aerosol model = urban type, atmospheric model = mid-latitude summer, SZ = 20°, VZ = 20°, and RA = 120°) and various LSR values (0.01, 0.08, 0.1 and 0.2).

commonly observed in the lower troposphere, which can influence satellite-measured radiances (He et al., 2008; Pashayi et al., 2025; Wang et al., 2025). Simulations were conducted, assuming a total AOD of 0.9, an urban aerosol type, and mid-latitude summer atmospheric conditions. A fixed observation geometry (SZ = 20°, VZ = 20°, and RA = 120°) was initially applied to isolate the impact of aerosol vertical distribution from geometric variations, given Himawari-8′s near-constant viewing angle over a fixed region.

The results indicate that increasing aerosol height (from H1 to H4) alters TOA reflectance, with the magnitude and direction of the effect depending on wavelength and land surface reflectance (LSR) (Fig. 2). In general, TOA reflectance increases with aerosol altitude when LSR < 0.2 but decreases when LSR = 0.2 due to the interplay of aerosol scattering and surface brightness. Among the profiles, H4 (with most aerosols at higher altitudes) produces the strongest satellite signal, while H1 has the weakest effect. Shortwave bands (B1 and B2) are more sensitive to changes in aerosol height than longer wavelengths. Notably, TOA reflectance in B3 and B4 tends to converge at higher altitudes (~3 km), whereas B1 retains clearer separation across vertical profiles, demonstrating its stronger sensitivity to vertical distribution. Overall, shifting aerosol concentration to higher altitudes consistently increases TOA reflectance, especially in shorter wavelength bands, partly due to stronger scattering near the top of the atmosphere and reduced absorption in bands such as O_2 A (760 nm) and B (687 nm). To further evaluate whether variations in viewing geometry could confound the interpretation of aerosol layer height, we conducted additional simulations of TOA reflectance for bands B1 and B4 across a range of solar zenith angles (20°–60°), viewing zenith angles (20°–60°), and relative azimuth angles (10°–150°) (Fig. S2). While TOA reflectance may overlap under different geometries for a given band, they remain distinguishable between different bands, confirming the feasibility of retrieving aerosol vertical distributions using Himawari-8′s multi-band observations under diverse observing conditions.

3.2. TF-FCNN model

In this study, two advanced deep learning models, the Transformer (Vaswani et al., 2017) and the Fully Connected Neural Network (FCNN) (Fan and Sun, 2023; Rumelhart et al., 1986), are integrated to enhance the model's ability to capture nonlinear relationships in retrieving aerosol properties from satellite imagery. Transformer, an encode-decode framework, has demonstrated strong information extraction capabilities, especially for localized and subtle features, making it a widely used feature extractor in natural language processing (NLP) tasks (Han et al., 2023; Wei et al., 2024). Its robustness and flexibility in training and application stem from three key modules, including multi-head attention, positional encoding, and residual blocks (Han et al., 2023; Vaswani et al., 2017). Here, we use two blocks within the decode module of the transformer model, which includes multi-head attention and residual modules, to construct and improve the model's training time and efficiency. Additionally, layer normalization is applied to maintain model stability and accelerate convergence during training. Finally, we integrate the FCNN model to further enhance the information extraction capability by fully utilizing the outputs of the Transformer model. FCNN consists of multiple neurons and hidden layers and is well-suited for quantitative retrieval tasks in remote sensing due to its strong ability to fit global features across different samples from satellite spectral bands (Fan and Sun, 2023; Fan et al., 2024). Our new hybrid framework comprises two stages:

Stage I: For the TF-FCNN model, we initially use the Transformer block as a local feature extractor to fit the nonlinear relationship between the CALIPSO measurements and the primary input predictors, which include the Himawari-8 TOA reflectance, MODIS BRDF features, as well as observation geometry. We decouple aerosols and surface signals by leveraging spectral differences across multiple channels spanning the visible, near-infrared, and shortwave infrared ranges.

Specifically, we use the TOA reflectance from the first six bands [i.e., B1 (0.47 μm), B2 (0.51 μm), B3 (0.64 μm), B4 (0.86 μm), B5 (1.6 μm) and B6 (2.3 μm)] as the key variables, as they are highly sensitive to aerosol's loadings as well as its vertical distributions. The BT data from the B14 band (11.2 μm) is also included as an input due to its ability to indicate high aerosol load conditions such as dust and smoke (Liu et al., 2024). Additionally, three BRDF parameters (i.e., ISO, VOI, and GEO) at blue (0.46 μm), green (0.55 μm), and red (0.65 μm) bands serve as indicators of surface conditions and are incorporated into the model. The three selected bands correspond to key wavelengths within the visible spectrum that are commonly used for aerosol optical property retrievals, balancing sensitivity to aerosol scattering and absorption while minimizing surface reflectance interference. The observation angles (SZ, VZ, and RA) are also added to the model to decouple aerosols and surface information using different spectral channels. The temporal feature, represented by the day of the year (DOY), is included to enhance performance, considering the short atmospheric lifespan of aerosols and the significant day-to-day variations (Wei et al., 2020), especially in regions with complex and transient aerosol sources, such as wildfires. Table S3 and Fig. S3 provide detailed information about the input variables and their distributions.

Stage II: The outputs of the f_{TF} are then inputted into the FCNN model (f_{FCNN}) to further learn and fit the complex relationship between the aerosol vertical distribution and the same set of variables, similar to the Transformer model, but in a global context. As a result, these two are deeply integrated to form the final TF-FCNN model $\{f_{FCNN}[f_{TF}(X)]\}$, which has a greater capability to simultaneously extract both global and local features from a total of 20 input variables compared to using a single model. The two stages work in parallel during the model training and can be represented as follows:

$$AEC_h = f_{FCNN}[f_{TF}\left(TOA_{\lambda_i}, BT, SA, SZ, RA, ISO_{\gamma_j}, VOL_{\gamma_j}, GEO_{\gamma_j}, DOY\right)] \quad (1)$$

where AEC_h represents the retrieved aerosol extinction coefficient at height h. λ_i and γ_j represent the B1-B6 bands of Himawari-8 and the B1-B3 bands of MODIS, respectively.

In this study, the TF-FCNN model is implemented and trained based on the Pytorch module in Python. Specifically, there are two blocks as well as 512 and 256 neurons that constitute the Transformer and FCNN parts of the TF-FCNN model, respectively. To enhance the model's stability and convergence speed during training, appropriate hyperparameters, and loss functions are determined by using a trial-and-error approach. After a lot of training, testing, and comparing, we finally selected the MSELoss as the loss function to the deviation between aerosols and satellite observations and used the Adam as the optimizer to avoid results falling into local optimality and speed up training.

3.3. Model interpretation and validation

Here, the SHapley Additive exPlanations (SHAP) (Lundberg and Lee, 2017) method is adopted to interpret the importance of each feature in deriving the aerosol vertical distribution using deep learning. SHAP is an advanced XAI technique that assigns a fair contribution value to each feature, ensuring consistency and transparency in how the model arrives at its predictions. It has unique advantages, including being model-agnostic, providing clear and interpretable insights into both global and local feature importance, and ensuring fairness by distributing contributions according to game-theoretic principles. SHAP has become a powerful tool for understanding and communicating the behavior of complex deep-learning models in related air quality tasks (Cheng et al., 2025; Wei et al., 2024). The SHAP analysis method is applied to interpret our trained deep-learning model. The SHAP values are calculated using the independent test set (20 % of total data samples), which is randomly split from the original data and is representative of the overall data distribution. This approach ensures that the interpretation reflects the model's behavior on unseen data, aligning with real-world

application scenarios. It also balances computational efficiency with statistical robustness while maintaining relevance to the model's generalization performance.

Three independent approaches are adopted to validate the model's performance: i.e., the sample-based 10-fold cross-validation (10-CV) is used to evaluate the overall accuracy of the TF-FCNN model in retrieving hourly aerosol vertical distributions, while time-based and space-based 10-CV are employed to access the model's predictive ability in areas and on dates where the truth values from CALIPSO observations are not available (Wei et al., 2023). Sample-based cross-validation refers to randomly dividing all data samples into 10 folds, with 9 folds used for training and the remaining one for validation in each iteration. Time-based cross-validation divides the data by day of the year into 10 temporal folds (i.e., 365 days grouped into 10 folds), with each fold used once as the test set while training on the remaining 9 folds. Space-based cross-validation involves dividing the study domain into approximately 658 $1° \times 1°$ grid cells, which are randomly grouped into 10 spatial folds. In each round, one fold is held out for validation while the model is trained on the remaining nine. This setup ensures that model performance is robustly assessed across random sampling, temporal variation, and spatial heterogeneity.

To further strengthen the spatial evaluation, we implement an additional stratified spatial partitioning scheme by dividing the sample sets into seven geographically distinct regions in Australia (Fig. S4), and then apply a leave-one-region-out cross-validation approach, in which one region is used for validation and the remaining regions for training. Lastly, given the absence of CALIPSO observations in other hours, we implemented a leave-one-hour-out cross-validation approach (Wei et al., 2024) to validate the model's performance in predicting different aerosol layer heights at unobserved times. In this approach, data samples from one hour were used for independent validation, while data samples from the remaining three hours were used for training.

The cross-validated coefficients of determination (R^2), correlation coefficient (R), root mean square error (RMSE), and mean absolute error (MAE) are used to quantitatively assess the model's performance and uncertainty. Note that the validation is performed for each hour during the period from 02:00 to 07:00 UTC.

4. Results and discussion

4.1. Model interpretation and feature analysis

The XAI − SHAP method is employed to evaluate the contribution of each feature on the retrieval of hourly aerosol vertical distributions from space using the developed TF-FTNN model (Fig. S5). At the low layer (i.e., 0.01–1 km), shortwave bands (B1 and B2) have significant impacts on the model, contributing ∼ 24 % to the outputs. This is attributed to aerosols exhibiting stronger extinction (e.g., scattering and absorption) of solar light at shorter wavelengths (e.g., blue) compared to longer wavelengths (e.g., shortwave infrared) (Hsu et al., 2013). Additionally, the thermal infrared band (B14) accounts for 9 % of the model's importance, likely due to its strong sensibility to high-loading aerosols, such as dust and smoke. Multiple BRDF features from various wavelengths exhibit a high cumulative contribution of 19 %, as they effectively explain the interaction between surface and solar light, influencing satellite signals at the top of the atmosphere. Observation geometry, particularly the VZ, has a substantial contribution (∼11 %) due to its strong correlations with satellite signals under varying surface and atmospheric conditions and its wide range of values (approximately from 0 to 90°) in the full-disc image for the geostationary satellites. The remaining variables collectively contribute 37 % to the retrieval, indicating their important auxiliary roles in the model. For the 1–2 km and 2–3 km layers, the contributions of these variables are similar to those at 0.01–1 km, with slight variations: B1 and B2 contribute ∼ 32.6 % and 39.58 %, B14 contributes ∼ 22 % and 17 %, BRDF contributes ∼ 14 % and 13 %, VZ contributes ∼ 8 % and 12 %, and the remaining variables

collectively contribute ∼ 25 % and 18 % of the model's final outputs, respectively. Overall, XAI provides unique insights into the physical connections within the deep learning model for aerosol vertical distribution retrieval and reveals that approximately 63 % of the contributions to the TF-FCNN model come from shortwave and bright temperature bands, as well as BRDF characteristics.

4.2. Validation of aerosol extinction coefficient retrievals

The TF-FCNN model is first validated using the sample-based 10-CV approach at three height layers in Australia (Fig. 3). The absence of data points in central Australia is due to the limited coverage of high-quality CALIPSO observations, as this region, dominated by vast deserts and bare land, restricts data availability. In space, the model demonstrates reliable retrievals in most regions of Australia at all three height layers, with an average high CV-R^2 (> 0.7) and low RMSE (< 0.1) across over 62 %, 61 %, and 62 % of the $1° \times 1°$ grids for the 0–1 km, 1–2 km, and 2–3 km layers, respectively (Fig. 3a–c). At the 0–1 km height, the hourly AEC retrievals (N = 77374) are highly consistent with CALIPSO measurements (CV-R^2 = 0.903), exhibiting low uncertainties, with an average RMSE of 0.037 and MAE of 0.018 across Australia in 2022 (Fig. 3d). At the 1–2 km and 2–3 km layers, the retrieval accuracy gradually worsens but still shows good consistency with CALIPSO measurements (CV-R^2 = 0.872 and 0.814, respectively), with average RMSEs (MAEs) of 0.031 (0.014) and 0.041 (0.023), respectively (Fig. 3e-f). However, the retrievals at these layers tend to be underestimated, potentially due to the smaller sample size of high-loading aerosol cases, but the bias is minimal, as evidenced by the strong line regression slopes (0.83–0.9). Our model performs well and remains relatively stable across different times of day (i.e., 04:00–07:00 UTC) at all height layers, with CV-R^2 ranging from 0.7 to 0.92 and RMSE ranging from 0.02 to 0.05 (Fig. 4). In addition, the combined TF-FCNN achieves better performance, improving the CV-R^2 by 4–6 % and reducing RMSE by 14–19 %, respectively, compared to the individual FCNN or Transformer models (Fig. S6).

Furthermore, our results show higher accuracy with BRDF inputs (CV-R^2 = 0.81–0.90) compared to without (CV-R^2 = 0.46–0.60) across different aerosol layers (Table S4). Importantly, including BRDF variables improves retrieval accuracy by over 10 % across different land-use types, particularly for forest and cropland (Fig. S7). This improvement is mainly because BRDF captures the anisotropic scattering of surface reflectance, which varies significantly with observation geometry and land cover types, particularly in forests and croplands. These land cover types exhibit high variability due to factors such as vegetation structure, leaf orientation, and canopy density, all of which strongly influence surface reflectance. By capturing these directional effects, BRDF features help account for such variability, leading to more accurate surface reflectance modeling. This, in turn, improves the model's ability to distinguish aerosol signals from surface background, enhancing retrieval accuracy in complex regions.

Moreover, we examine the spatial and temporal predictive ability of our model in retrieving aerosol extinction coefficient retrievals using the space- and time-based 10-CV methods in Australia. In general, over 60 % of regions across the domain show good grid-based CV-R^2 (> 0.5) and low RMSE values (< 0.1) for all height layers (Fig. S8a-c). The model performs well at the low height level (0–1 km) where CALIPSO measurements are unavailable (i.e., CV-R^2 = 0.636 and RMSE = 0.072), and shows comparable predictive abilities at 1–2 km and 2–3 km (CV-R^2 = 0.579 and 0.51, RMSE = 0.056 and 0.057) (Fig. S8d-f). The predictions are relatively stable over time, but accuracy slightly decreases with increasing height layers, likely due to varying aerosol transport and vertical distributions across Australia, with moderate CV-R^2 values ranging from 0.43 to 0.68 (Fig. S9).

The day-based CV results showed a similar spatial pattern to grid-based CV, with good AEC retrievals (i.e., CV-R^2 > 0.5 and RMSE < 0.1) at the same 60 % of grids across Australia (Fig. S10a-c). These
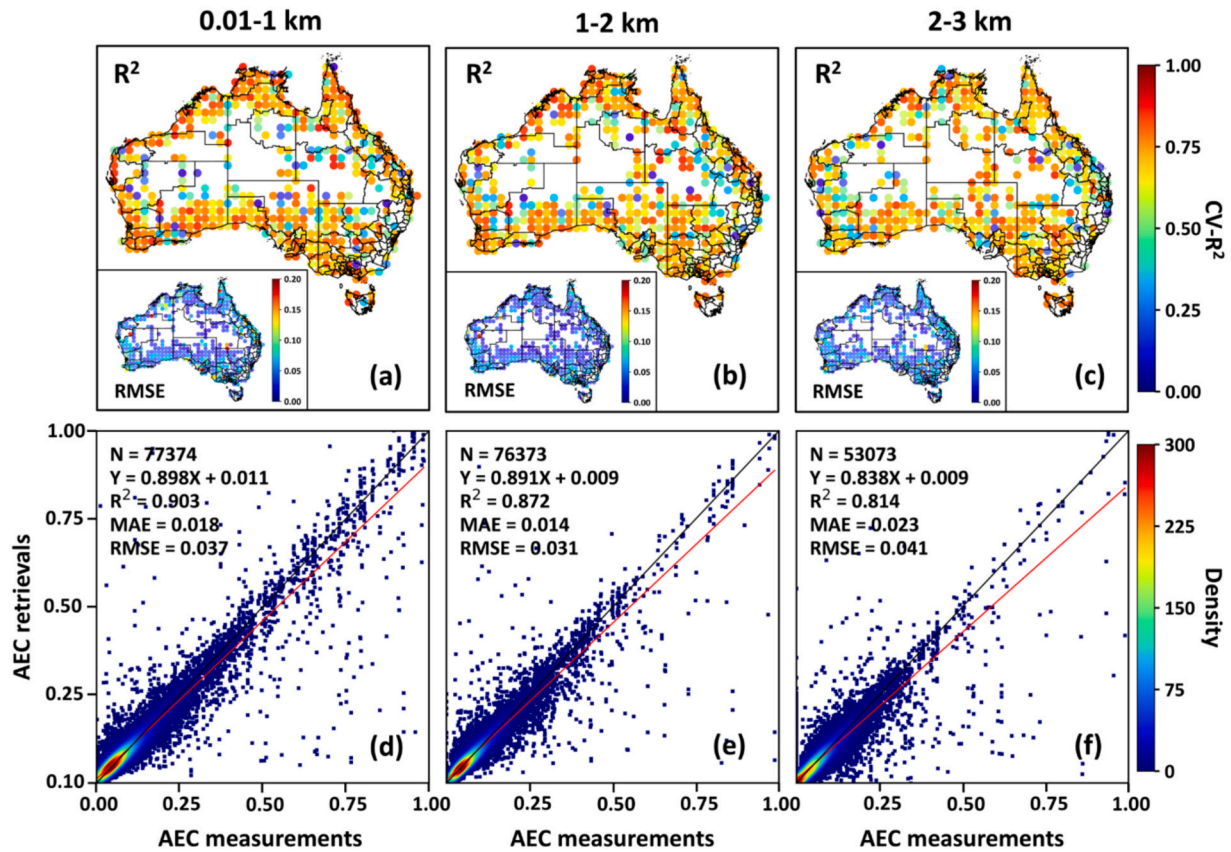
Fig. 3. Overall accuracy and uncertainty distribution (a-c) at each $1° \times 1°$ grid in Australia and (d-f) density scatter plot between our hourly (from 02:00 to 07:00 UTC) aerosol extinction coefficient (AEC) retrievals and CALIPSO AEC measurements at three height levels (0–1 km, 1–2 km, and 2–3 km) in 2022, using the sample-based 10-CV approach. The black line represents the 1:1 line, and the red line represents the fitted line. (For interpretation of the references to colour in this figure legend, the reader is referred to the web version of this article.)

results demonstrate the model's reliable ability to provide aerosol vertical distribution information at moments without CALIPSO measurements (i.e., CV-R^2 = 0.68–0.78 and RMSE = 0.04–0.06; Fig. S10d-f). Temporal predictions of the model are relatively reliable at varying hours, with CV-R^2 ranging from 0.6 to 0.86, except for the early hour (04:00 UTC), where the much smaller number of data samples leads to reduced accuracy (Fig. S11). Overall, the predictive accuracy is generally lower than the estimated accuracy but does not drop significantly (~15 %), and these comprehensive validation results demonstrate acceptable AEC retrievals for studying aerosol vertical distributions at different heights in Australia.

Lastly, our model also demonstrates consistent performance across different validation hours (R = 0.64–0.79) with low variability (RMSE = 0.05–0.08), showing only slight decreases when extended to earlier or later times using the leave-one-hour-out cross-validation approach (Table S5). This indicates overall stable temporal generalizability and suggests that our model effectively captures temporal features and is minimally sensitive to diurnal sampling bias. Moreover, our model demonstrates consistent predictive skill in retrieving aerosol vertical distributions across different altitudes, as evidenced by moderate to high correlations (R = 0.41–0.77) and relatively low uncertainties (RMSE = 0.07–0.15) across all regions using the leave-one-region-out crossing validation (Table S6). These results illustrate our model's strong spatial and temporal ability to retrieve reliable aerosol layer heights.

4.3. Diurnal variations in aerosol vertical distributions

Anthropogenic emissions from urban areas can significantly alter aerosol distribution at various heights, making the study of aerosol vertical distribution crucial for air pollution control. Using our TF-FCNN

model, we first provide the spatially continuous hourly aerosol vertical distributions from 02:00 to 07:00 UTC in Australia, highlighting their diurnal variation in densely populated urban areas (Fig. 5). On February 14, 2022, the aerosol loading (average = ~0.14 ± 0.05) at 0.01–1 km is notably higher than at 1–2 km (~0.11 ± 0.04) and 2–3 km (~0.07 ± 0.03), reflecting the typical upward transport of aerosols from ground-level emissions. In major urban areas like Canberra, this difference between 0.01–1 km and 2–3 km is even more pronounced at 71 % due to the increase in the contributions of human activities to aerosols. At 0.01–1 km, aerosols, mainly from human emissions such as industry and transportation (Froehlich et al., 2015), are typically precursors in the form of fine particulate matter (e.g., $PM_{2.5}$), which can contribute heavy urban haze and pose high health risks (Feng et al., 2024; Shiraiwa et al., 2017). In contrast, the lower aerosol concentrations at 1–2 km and 2–3 km are possibly due to their more widespread aerosol dispersion and transmission to the surrounding areas (Li et al., 2022). Additionally, the diurnal relative variation of aerosols at 0.01–1 km (~20 %) is much greater than at 1–2 km (~17 %) and 2–3 km (~5%), with more pronounced around Canberra. Specifically, the averaged AEC for core urban areas of Canberra (a window of 10×10 pixels) at 0–1 km is 0.17 at 2:00 and decreases to 0.08 after five hours, representing a more than 52 % reduction. In comparison, the averaged AECs at 1–2 km (2–3 km) are 0.12 (0.09) at 2:00 and 0.08 (0.07) at 7:00, reflecting a 35 % (21 %) change. Similar spatiotemporal differences and variations in aerosol vertical distribution were also observed during different heavy urban haze events, such as on July 15, 2022, in Canberra (Fig. S12) and on January 21, 2022, in Melbourne (Fig. S13).

Wildfires are a major natural pollutant source affecting aerosol vertical distributions, especially considering the significant increase in wildfire emissions in Australia in recent years (Boer et al., 2020;
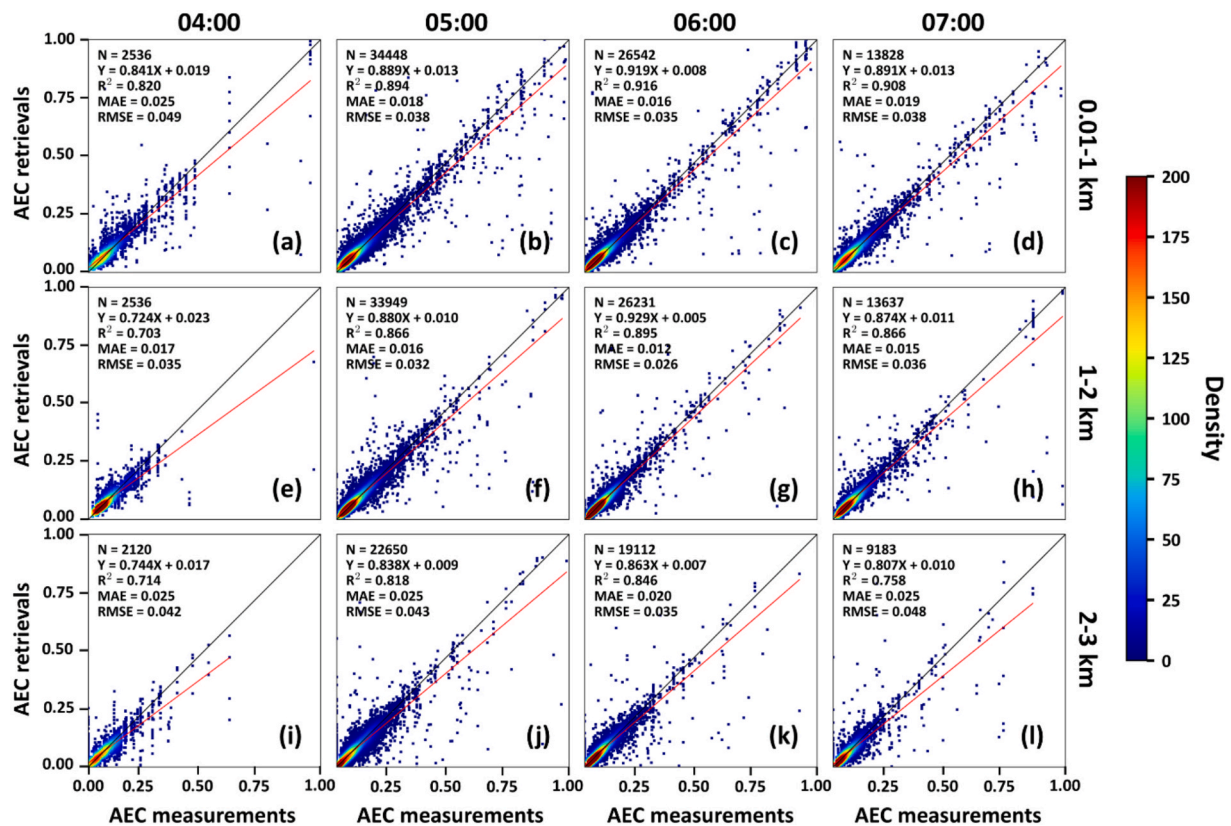
Fig. 4. Density scatter plots between our aerosol extinction coefficient (AEC) retrievals and CALIPSO AEC measurements at (a-d) 0–1 km, (e-h) 1–2 km, and (i-l) 2–3 km from 04:00 to 07:00 UTC in 2022, using the sample-based 10-CV approach. The black line represents the 1:1 line, and the red line represents the fitted line. (For interpretation of the references to colour in this figure legend, the reader is referred to the web version of this article.)

Richardson et al., 2022; Salawitch and McBride, 2022). In this study, we provide unique insights into both the vertical and horizontal transport of smoke particles from the ground to the upper atmosphere by offering hourly aerosol extinction coefficients at different heights. On February 7, 2022, significant wildfire activities (indicated by red dots extracted from the MOD14A1 fire product) in both western and eastern Australia led to a notable increase in aerosol loads at all height layers (Fig. 6). For example, the 0.01–1 km AECs exhibited significantly higher levels near the fire regions (a window of 10×10 pixels), showing an increase of $\sim$ 30 % compared to the 1–2 km layer (average = 0.16 ± 0.04) during 02:00–07:00 UTC. In contrast, aerosols in the 2–3 km layer continued to reduce slightly by $\sim$ 25 % over the same period. The changes at 0.01–1 km and 1–2 km are more dramatic than those in urban haze caused by human emissions, particularly at the temporal scale, as aerosol loads increase significantly over time due to the rapid growth and spread of the fires. Our retrievals successfully capture these strong diurnal variations caused by wildfires: prior to 5:00, aerosol loads remained relatively steady, with relative changes of 5 % for 0.01–1 km, 7 % for 1–2 km, and 4 % for 2–3 km, respectively. In contrast, between 4:00–5:00, aerosol levels suddenly increase by 29 %, 22 %, and 21 % at the three heights. After 5:00, aerosols continued to increase at 0.01–1 km and 1–2 km by 36 % and 39 %, while the 2–3 km aerosols decreased by 53 %. By contrast, CALIPSO cannot provide timely aerosol changes during wildfires, as it only passes over Australia once or twice a day. As most wildfires occur in densely vegetated areas on the ground, they initially release large amounts of smoke and dust into the lower atmosphere. This leads to increased AECs at 0.01–1 km, with some dispersion to the 1–2 km layer. However, aerosol concentrations in the 2–3 km layer decrease, likely because wildfire smoke is not strong enough to reach such high altitudes and because of the stronger diffusion and sedimentation at higher altitudes. A similar conclusion can be drawn from other wildfire

events that occurred on January 19, 2022, in Northwestern Austria (Fig. S14) and on January 21, 2022, in Southeastern Austria (Fig. S15).

Last, we compare our retrievals (black) with CALIPSO measurements (red) as a function of latitude for the 0.01–1 km, 1–2 km, and 2–3 km layers under the aforementioned polluted conditions (Fig. S16). It is clear that our aerosol extinction coefficient retrievals closely align with individual CALIPSO measurements taken at discrete locations under both the urban haze and wildfire conditions ($R^2 = 0.96$ and 0.92) while also providing critical aerosol vertical profile information in regions where CALIPSO measurements are typically absent. More importantly, our retrievals offer greater spatial continuity than the CALIPSO measurements, which provide limited coverage with fewer than two observations per day across the domain and are sometimes hindered by low signal-to-noise ratio and invalid observations (Kim et al., 2018; Mao et al., 2022; Tackett et al., 2023). Therefore, these results further demonstrate the suitability of our unique approach for studying aerosol vertical distributions across vast regions, particularly under highly polluted conditions.

4.4. Comparison with previous studies

Compared with previous studies on aerosol vertical distribution estimation (Table 1), our proposed TF-FCNN model demonstrates clear advantages in both spatiotemporal resolutions and accuracy. Most earlier approaches are often limited by coarse temporal coverage, typically providing annual estimates from MODIS (Kudo et al., 2023; Li et al., 2025) or multi-day estimates from SCIAMACHY (Scanning Imaging Absorption Mpectrometer for Atmospheric CHartographY) (Sanghavi et al., 2012) and OCO-2 (Wang et al., 2025). Even studies using (TROPOMI (TROPOspheric Monitoring Instrument) or GOME-2A (Global Ozone Monitoring Experiment–2 onboard MetOp-A) (Chen
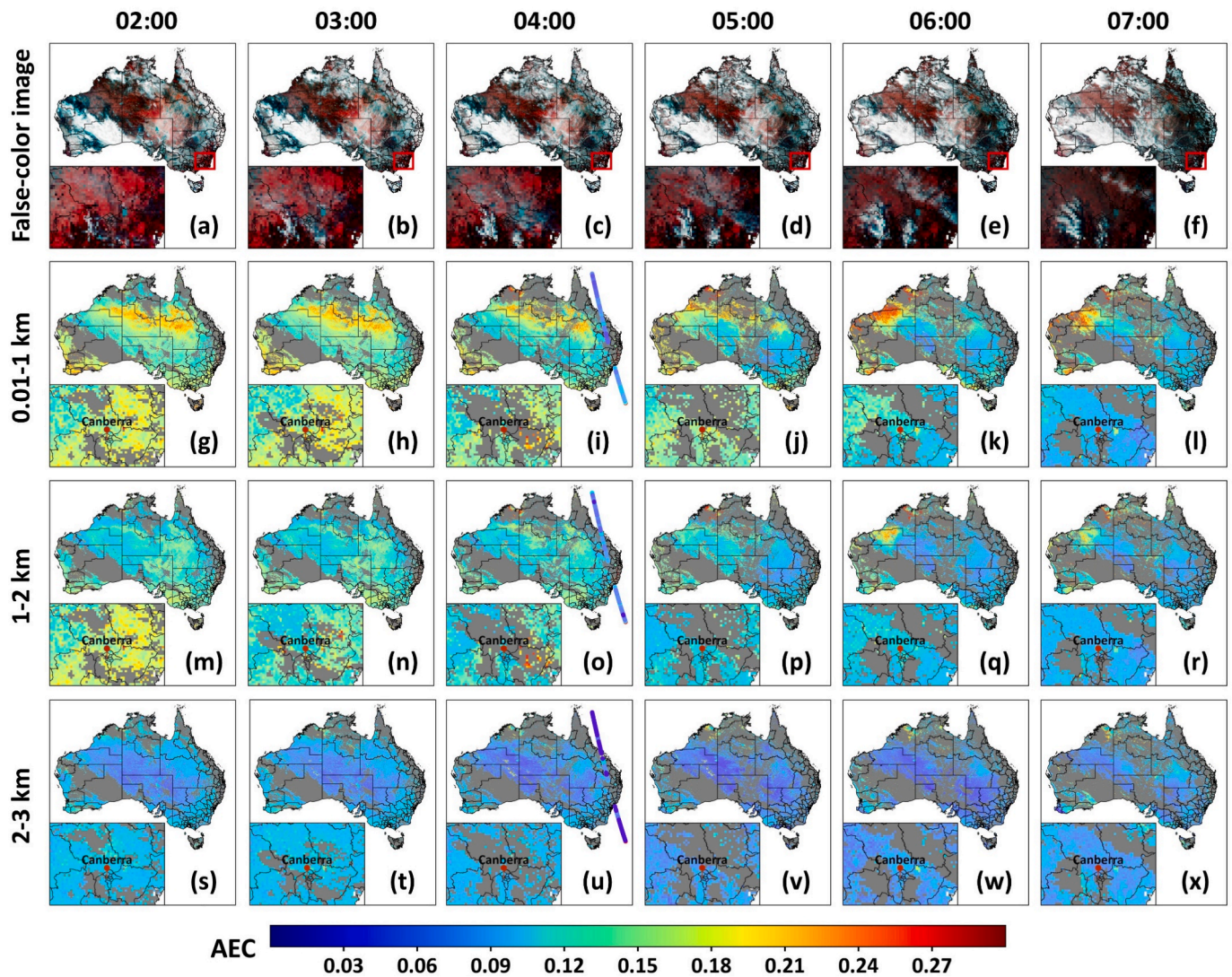
Fig. 5. Diurnal variations in aerosol vertical distributions across Australia, showing aerosol extinction coefficient (AEC) retrievals at different heights (0–1 km, 1–2 km, and 2–3 km) from 02:00 to 07:00 UTC on February 14, 2022. The red rectangle highlights the zoomed-in urban region around Canberra in Southeastern Australia during a heavy haze event. The colored dots represent the available CALIPSO AEC observations crossing the domain. (For interpretation of the references to colour in this figure legend, the reader is referred to the web version of this article.)

et al., 2021; Lemmouchi et al., 2022; Maheshwarkar et al., 2024; Sanders et al., 2015) data are typically constrained to daily resolution. In contrast, our approach leverages high-temporal-frequency Himawari-8 geostationary observations to generate hourly estimates at the highest 2 km spatial resolution, finer than the 3-hour, 10-km resolution estimates derived from EPIC (Earth Polychromatic Imaging Camera) observations (Xu et al., 2019) and hourly, 3-km resolution estimates from SEVIRI observations (Pashayi et al., 2025).

In terms of accuracy, our model achieves an average R^2 of 0.88, outperforming most existing methods, including Look-Up-Table-based approaches (0.52–0.76; Chen et al., 2021; Xu et al., 2019), Spectral Fit methods (R^2 = 0.41–0.76; Maheshwarkar et al., 2024; Sanders et al., 2015), AEROS5P (R^2 = 0.69; Lemmouchi et al., 2022), and Optimal Estimation Techniques (R^2 = 0.73; Kudo et al., 2023). Our model also performs better than recent machine learning models (R^2 = 0.79–0.86), such as LSTM-TF (Wang et al., 2025), XLW (Li et al., 2025), and XGBoost (Pashayi et al., 2025) models. These improvements stem from the TF-FCNN's unique integration of temporal fusion and spatial feature learning, enabled by combining advanced deep learning architectures with additional physical factors (e.g., BRDF parameters), allowing for a more effective representation of complex spatiotemporal patterns in

aerosol vertical structures.

5. Conclusions

Aerosol vertical distributions are highly valuable for studying particle transport, but obtaining them with spatial continuity and timeliness is very challenging, especially when relying solely on active Lidar observations. To address this, we introduced a novel aerosol vertical distribution retrieval framework that combines two deep-learning models (Transformer + FCNN) to enhance the extraction of global and local features during nonlinear relationship building and produce hourly aerosol vertical distributions from multi-source satellite data (including CALIPSO, Himawari-8, and MODIS). An XAI-based SHAP approach is employed to quantify each variable importance and reveal the physical connections within the deep learning model. The model's performance is comprehensively validated using various spatiotemporal cross-validation approaches to ensure the reliability of the retrievals.

We find that the Himawari-8 shortwave band TOA reflectance (0.45 μm and 0.51 μm) contributed approximately 32 %, while the BT (11.2 μm) contributed ∼ 16 % to the hourly aerosol extinction coefficient retrievals across Australia. Ten-fold cross-validations at random, daily,
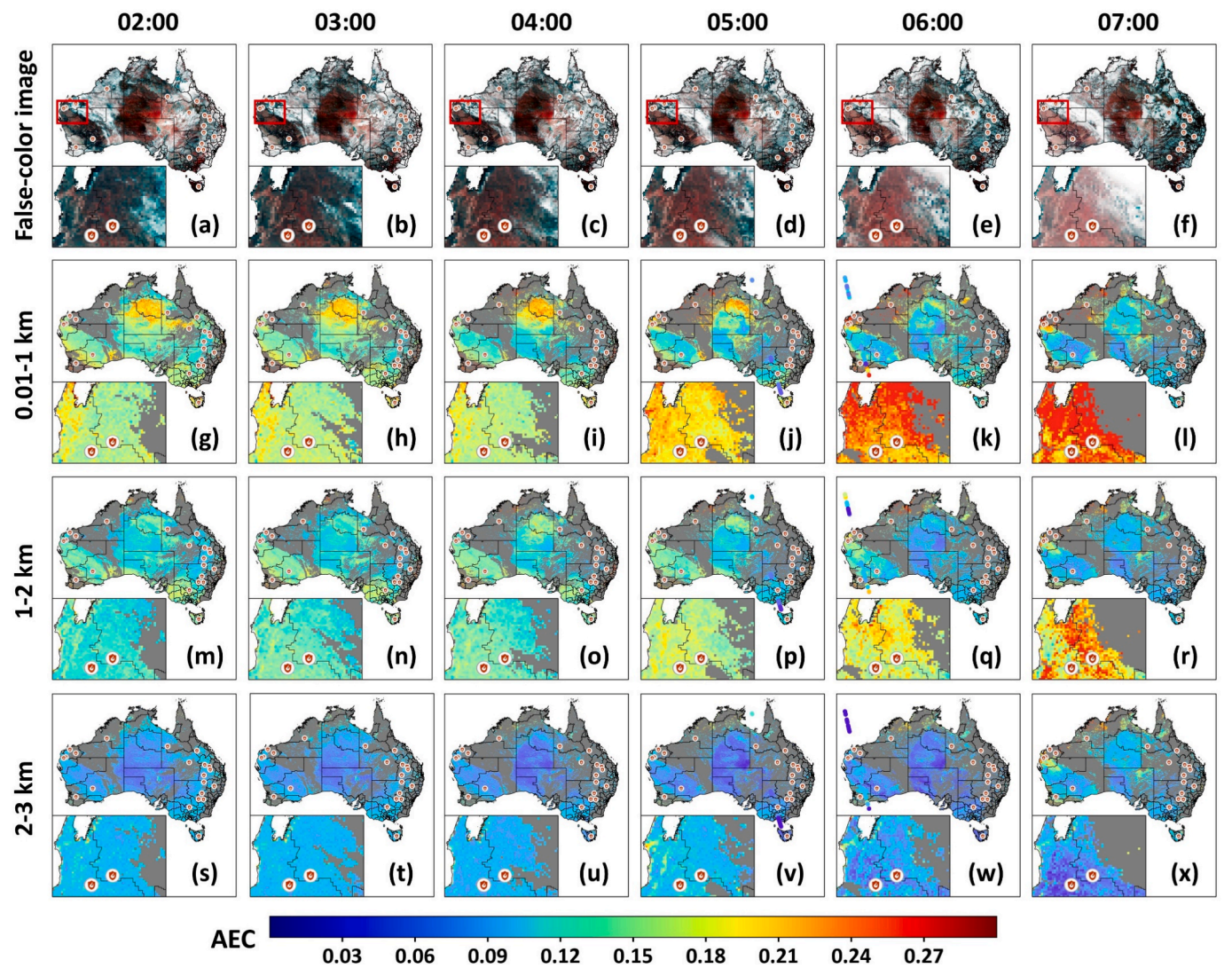
Fig. 6. Diurnal variations in aerosol vertical distributions during a heavy wildfire event across Australia, showing aerosol extinction coefficient (AEC) retrievals at different heights (0–1 km, 1–2 km, and 2–3 km) from 02:00 to 07:00 UTC on February 7, 2022. The red rectangle highlights the zoomed-in region with widespread wildfires in Western Australia. The fire circle symbols indicate fire points extracted from the MOD14A1 fire product, and colored dots indicate the available CALIPSO AEC observations crossing the domain. (For interpretation of the references to colour in this figure legend, the reader is referred to the web version of this article.)

Table 1
Comparison with previous studies on aerosol vertical distribution estimation.

Model	Accuracy (CV-R^2)	Satellite sensor	Spatial resolution	Temporal resolution	Reference
OST	0.73	MODIS	50 × 20 km	Annual	Kudo et al. (2023)
XLW	0.84–0.85	MODIS	5 × 5 km	Annual	Li et al. (2025)
LSTM-TF	0.79	OCO-2	2.25 × 1.29 km	16-day	Wang et al. (2025)
OST	0.85	SCIAMACHY	30 × 60 km	6-day	Sanghavi et al. (2012)
SF	0.41	GOME-2A	40 × 40 km	Daily	Sanders et al. (2015)
LUT	0.76	TROPOMI	3.5 × 5.5 km	Daily	Chen et al. (2021)
AEROS5P	0.69	TROPOMI	3.5 × 5.5 km	Daily	Lemmouchi et al. (2022)
SF	0.76	TROPOMI	3.5 × 5.5 km	Daily	Maheshwarkar et al. (2024)
LUT	0.72	EPIC	10 × 10 km	3-hour	Xu et al. (2019)
XGBoost	0.59–0.86	SEVIRI	3 × 3 km	Hourly	Pashayi et al. (2025)
TF-FCNN	0.88	Himawari-8	2 × 2 km	Hourly	This study

LSTM-TF: Long Short-Term Memory and Transformer model; LUT: Look-Up-Tale approach; OST: Optimal Estimation Technique; SF: Spectral Fit; XLW: XGBoost-LightGBM-Wavelet model.

and gridded levels demonstrate the robust performance of the model at different heights (0.01–1 km, 1–2 km, and 2–3 km) and hours (02:00–07:00 UTC) throughout the day, achieving high overall accuracy (e.g., CV-R^2 = 0.81–0.9, RMSE = 0.031–0.041) and strong predictive capabilities in areas (e.g., CV-R^2 = 0.51–0.64, RMSE = 0.056–0.072) as well as on dates (e.g., CV-R^2 = 0.69–0.78, RMSE = 0.044–0.057) where CALIPSO observations are not available. The TF-FCNN demonstrated superior feature extraction ability compared to individual FCNN and

Transformer models. We applied this model to generate and analyze aerosol vertical distributions and variations over Australia during haze and wildfire events, revealing higher aerosol loading at lower altitudes in core urban and wildfire regions due to anthropogenic and smoke emissions, with more significant changes observed at 0.01–1 km compared to higher layers (1–3 km). Additionally, the model successfully captured strong diurnal aerosol variability on individual days, particularly the increasing aerosol loadings over time driven by the spread and intensification of wildfires.

In general, our study first provides unique insights into hourly aerosol vertical distributions, a task very challenging for CALIPSO due to its 16-day revisit time. Nevertheless, limitations exist in our study, particularly regarding inherent uncertainties in CALIPSO aerosol observations. Additionally, the current use of three limited layers restricts the ability to study finer aerosol vertical distributions, particularly in regions with significant aerosol variations. Therefore, we will extend our deep-learning framework to retrieve aerosol distributions across finer vertical layers in future work to better support the research community. In addition, we will extend our analysis to more complex regions, such as East Asia, which exhibit higher aerosol loadings and more complex pollution mixtures, to further assess our model's robustness and adaptability across varying aerosol regimes. Based on this, an in-depth quantitative analysis of aerosol variability drivers, including both meteorological and anthropogenic factors during heavy pollution episodes, will be explored to advance the understanding of aerosol vertical distributions and their variability on short-term scales in our future studies.

CRediT authorship contribution statement

Yulong Fan: Writing – review & editing, Writing – original draft, Visualization, Validation, Software, Methodology, Data curation. **Lin Sun:** Writing – review & editing, Supervision, Project administration, Methodology, Funding acquisition, Formal analysis. **Zhihui Wang:** Writing – review & editing. **Shulin Pang:** Writing – review & editing. **Jing Wei:** Writing – review & editing, Supervision, Methodology.

Declaration of competing interest

The authors declare that they have no known competing financial interests or personal relationships that could have appeared to influence the work reported in this paper.

Acknowledgments

Appendix A. Supplementary data

Supplementary data to this article can be found online at https://doi.org/10.1016/j.isprsjprs.2025.08.021.

Data availability

The Himawari-8 L1 full-disk data is available at https://www.eorc.jaxa.jp/. The CALIPSO Level 2 Aerosol Profile product is available at https://search.earthdata.nasa.gov/. The MCD19A3D and MCD12Q1 Collection 6.1 products are available at https://ladsweb.modaps.eosdis.nasa.gov/, and MOD14A1 fire data is available at https://firms.modaps.eosdis.nasa.gov/.

References

Adams, A.M., Prospero, J.M., Zhang, C., 2012. CALIPSO-derived three-dimensional structure of aerosol over the atlantic basin and adjacent continents. J. Clim. 25, 6862–6879. https://doi.org/10.1175/JCLI-D-11-00672.1.

Boer, M.M., Resco de Dios, V., Bradstock, R.A., 2020. Unprecedented burn area of Australian mega forest fires. Nat. Clim. Chang. 10, 171–172. https://doi.org/10.1038/s41558-020-0716-1.

Campbell, J.R., Hlavka, D.L., Welton, E.J., Flynn, C.J., Turner, D.D., Spinhirne, J.D., Scott, V.S., Hwang, I.H., 2002. Full-time, eye-safe cloud and aerosol lidar observation at atmospheric radiation measurement program sites: instruments and data processing. J. Atmos. Ocean. Technol. 19, 431–442. https://doi.org/10.1175/1520-0426(2002)019<0431:FTESCA>2.0.CO;2.

Chen, B., Song, Z., Pan, F., Huang, Y., 2022. Obtaining vertical distribution of PM$_{2.5}$ from CALIOP data and machine learning algorithms. Sci. Total Environ. 805, 150338. https://doi.org/10.1016/j.scitotenv.2021.150338.

Chen, X., Wang, J., Xu, X., Zhou, M., Zhang, H., Castro Garcia, L., Colarco, P.R., Janz, S. J., Yorks, J., McGill, M., Reid, J.S., de Graaf, M., Kondragunta, S., 2021. First retrieval of absorbing aerosol height over dark target using TROPOMI oxygen B band: Algorithm development and application for surface particulate matter estimates. Remote Sens. Environ. 265, 112674. https://doi.org/10.1016/j.rse.2021.112674.

Cheng, F., Li, Z., Yang, Z., Li, R., Wang, D., Jia, A., Li, K., Zhao, B., Wang, S., Yin, D., Li, S., Xue, W., Cribb, M., Wei, J., 2025. First retrieval of 24-hourly 1-km-resolution gapless surface ozone (O$_3$) from space in China using artificial intelligence: Diurnal variations and implications for air quality and phytotoxicity. Remote Sens. Environ. 316, 114482. https://doi.org/10.1016/j.rse.2024.114482.

Choi, W., Lee, H., Kim, J., Ryu, J.-Y., Park, S.S., Park, J., Kang, H., 2019. Effects of spatiotemporal O$_4$ column densities and temperature-dependent O$_4$ absorption cross-section on an aerosol effective height retrieval algorithm using the O$_4$ air mass factor from the ozone monitoring instrument. Remote Sens. Environ. 229, 223–233. https://doi.org/10.1016/j.rse.2019.05.001.

Fan, Y., Sun, L., 2023. Satellite aerosol optical depth retrieval based on fully connected neural network (FCNN) and a combine algorithm of simplified aerosol retrieval algorithm and simplified and robust surface reflectance estimation (SREMARA). IEEE J. Sel. Top. Appl. Earth Obs. Remote Sens. 16, 4947–4962. https://doi.org/10.1109/JSTARS.2023.3281777.

Fan, Y., Sun, L., Liu, X., 2024. Data integration for ML-CNPM$_{2.5}$: a public sample dataset based on machine learning models and remote sensing technology applied for estimating ground-level PM$_{2.5}$ in China. IEEE Trans. Geosci. Remote Sens. 62, 1–15. https://doi.org/10.1109/TGRS.2024.3436006.

Feng, Y., Castro, E., Wei, Y., Jin, T., Qiu, X., Dominici, F., Schwartz, J., 2024. Long-term exposure to ambient PM$_{2.5}$, particulate constituents and hospital admissions from non-respiratory infection. Nat. Commun. 15, 1518. https://doi.org/10.1038/s41467-024-45776-0.

Froehlich, M., Chatterjee, S., Li, M., DeSilva, T., McDonald, J., Rockliff, S., Firkins-Fox, I., 2015. Airborne particulate matter pollution in the Australian capital Territory. Technical Report – Chemical Composition and Source. ACT (https://www.act.gov.au/).

Getzewich, B.J., Vaughan, M.A., Hunt, W.H., Avery, M.A., Powell, K.A., Tackett, J.L., Winker, D.M., Kar, J., Lee, K.P., Toth, T.D., 2018. CALIPSO lidar calibration at 532 nm: version 4 daytime algorithm. Atmos. Meas. Tech. 11, 6309–6326. https://doi.org/10.5194/amt-11-6309-2018.

Gupta, G., Ratnam, M.V., Madhavan, B.L., Prasad, P., Narayanamurthy, C.S., 2021. Vertical and spatial distribution of elevated aerosol layers obtained using long-term ground-based and space-borne lidar observations. Atmos. Environ. 246, 118172. https://doi.org/10.1016/j.atmosenv.2020.118172.

Han, K., Wang, Y., Chen, H., Chen, X., Guo, J., Liu, Z., Tang, Y., Xiao, A., Xu, C., Xu, Y., Yang, Z., Zhang, Y., Tao, D., 2023. A Survey on Vision Transformer. IEEE Trans. Pattern Anal. Mach. Intell. 45, 87–110. https://doi.org/10.1109/TPAMI.2022.3152247.

He, Q., Li, C., Mao, J., Lau, A.-K.-H., Chu, D.A., 2008. Analysis of aerosol vertical distribution and variability in Hong Kong. J. Geophys. Res. Atmos. 113, D14211. https://doi.org/10.1029/2008JD009778.

Heinold, B., Baars, H., Barja, B., Christensen, M., Kubin, A., Ohneiser, K., Schepanski, K., Schutgens, N., Senf, F., Schrödner, R., Villanueva, D., Tegen, I., 2022. Important role of stratospheric injection height for the distribution and radiative forcing of smoke aerosol from the 2019–2020 Australian wildfires. Atmos. Chem. Phys. 22, 9969–9985. https://doi.org/10.5194/acp-22-9969-2022.

Hsu, N., Jeong, M.J., Bettenhausen, C., Sayer, A., Hansell, R., Seftor, C., Huang, J., Tsay, S.C.J.J.o.G.R.A., 2013. Enhanced deep blue aerosol retrieval algorithm: The second generation. J. Geophys. Res. Atmos. 118, 9296-9315. DOI: 10.1002/jgrd.50712.

Huang, J., Guo, J., Wang, F., Liu, Z., Jeong, M.-J., Yu, H., Zhang, Z., 2015. CALIPSO inferred most probable heights of global dust and smoke layers. J. Geophys. Res. Atmos. 120, 5085–5100. https://doi.org/10.1002/2014JD022898.

Jiang, J., Tao, M., Xu, X., Jiang, Z., Man, W., Wang, J., Wang, L., Wang, Y., Zheng, Y., Tao, J., Chen, L., 2023. A generalized aerosol algorithm for multi-spectral satellite measurement with physics-informed deep learning method. Geophys. Res. Lett. 50, e2023GL106806. https://doi.org/10.1029/2023GL106806.

Kim, M.H., Omar, A.H., Tackett, J.L., Vaughan, M.A., Winker, D.M., Trepte, C.R., Hu, Y., Liu, Z., Poole, L.R., Pitts, M.C., Kar, J., Magill, B.E., 2018. The CALIPSO version 4 automated aerosol classification and lidar ratio selection algorithm. Atmos. Meas. Tech. 11, 6107–6135. https://doi.org/10.5194/amt-11-6107-2018.

Kotchenova, S.Y., Vermote, E.F., Levy, R., Lyapustin, A., 2008. Radiative transfer codes for atmospheric correction and aerosol retrieval: intercomparison study. Appl. Opt. 47, 2215–2226. https://doi.org/10.1364/AO.47.002215.

Kudo, R., Higurashi, A., Oikawa, E., Fujikawa, M., Ishimoto, H., Nishizawa, T., 2023. Global 3-D distribution of aerosol composition by synergistic use of CALIOP and MODIS observations. Atmos. Meas. Tech. 16, 3835–3863. https://doi.org/10.5194/amt-16-3835-2023.

Lee, W.R., Visioni, D., Bednarz, E.M., MacMartin, D.G., Kravitz, B., Tilmes, S., 2023. Quantifying the efficiency of stratospheric aerosol geoengineering at different altitudes. Geophys. Res. Lett. 50, e2023GL104417. https://doi.org/10.1029/2023gl104417.

Lemmouchi, F., Cuesta, J., Eremenko, M., Derognat, C., Siour, G., Dufour, G., Sellitto, P., Turquety, S., Tran, D., Liu, X., Zoogman, P., Lutz, R., Loyola, D., 2022. Three-dimensional distribution of biomass burning aerosols from Australian wildfires observed by TROPOMI satellite observations. Remote Sens. 14, 2582. https://doi.org/10.3390/rs14112582.

Li, J., Carlson, B.E., Yung, Y.L., Lv, D., Hansen, J., Penner, J.E., Liao, H., Ramaswamy, V., Kahn, R.A., Zhang, P., Dubovik, O., Ding, A., Lacis, A.A., Zhang, L., Dong, Y., 2022. Scattering and absorbing aerosols in the climate system. Nat. Rev. Earth Environ. 3, 363–379. https://doi.org/10.1038/s43017-022-00296-7.

Li, W., Han, W., Meng, J., Dong, Z., Xu, J., Wang, Q., Yuan, L., Wang, H., Zhang, Z., Cheng, M., 2025. Machine learning-based generation of high-resolution 3D full-coverage aerosol distribution data over China using multisource data. Remote Sens. Environ. 324, 114772. https://doi.org/10.1016/j.rse.2025.114772.

Liao, T., Gui, K., Li, Y., Wang, X., Sun, Y., 2021. Seasonal distribution and vertical structure of different types of aerosols in southwest China observed from CALIOP. Atmos. Environ. 246, 118145. https://doi.org/10.1016/j.atmosenv.2020.118145.

Liu, G., Li, J., Li, J., Yue, S., Zhou, R., 2024. Estimation of nighttime aerosol optical depths using atmospheric infrared sounder longwave radiances. Geophys. Res. Lett. 51, e2023GL108120. https://doi.org/10.1029/2023GL108120.

Lundberg, S.M., Lee, S.-I., 2017. A unified approach to interpreting model predictions, Proceedings of the 31st International Conference on Neural Information Processing Systems. Curran Associates Inc., Long Beach, California, USA, pp. 4768–4777.

Lyapustin, A., Wang, Y., Korkin, S., Huang, D., 2018. MODIS Collection 6 MAIAC algorithm. Atmos. Meas. Tech. 11, 5741–5765. https://doi.org/10.5194/amt-11-5741-2018.

Maheshwarkar, P., Cuesta, J., Formenti, P., Lemmouchi, F., 2024. Three-dimensional distribution of aerosols of multiple types at daily scale using TROPOMI spaceborne observations. Sci. Total Environ. 955, 177037. https://doi.org/10.1016/j.scitotenv.2024.177037.

Mao, F., Shi, R., Rosenfeld, D., Pan, Z., Zang, L., Zhu, Y., Lu, X., 2022. Retrieving instantaneous extinction of aerosol undetected by the CALIPSO layer detection algorithm. Atmos. Chem. Phys. 22, 10589–10602. https://doi.org/10.5194/acp-22-10589-2022.

NASA/LARC/SD/ASDC. (2018). CALIPSO Lidar Level 2 Aerosol Profile, V4-20 [Data set]. NASA Langley Atmospheric Science Data Center DAAC. Retrieved from https://doi.org/10.5067/CALIOP/CALIPSO/LID_L2_05KMAPRO-STANDARD-V4-20.

Pappalardo, G., Amodeo, A., Apituley, A., Comeron, A., Freudenthaler, V., Linné, H., Ansmann, A., Bösenberg, J., D'Amico, G., Mattis, I., Mona, L., Wandinger, U., Amiridis, V., Alados-Arboledas, L., Nicolae, D., Wiegner, M., 2014. EARLINET: Towards an advanced sustainable European aerosol lidar network. Atmos. Meas. Tech. 7, 2389–2409. https://doi.org/10.5194/amt-7-2389-2014.

Pashayi, M., Satari, M., Momeni Shahraki, M., 2025. Multi-layer retrieval of aerosol optical depth in the troposphere using SEVIRI data: a case study of the European continent. Atmos. Meas. Tech. 18, 1415–1439. https://doi.org/10.5194/amt-18-1415-2025.

Richardson, D., Black, A.S., Irving, D., Matear, R.J., Monselesan, D.P., Risbey, J.S., Squire, D.T., Tozer, C.R., 2022. Global increase in wildfire potential from compound fire weather and drought. npj Clim. Atmos. Sci. 5, 23. https://doi.org/10.1038/s41612-022-00248-4.

Rumelhart, D.E., Hinton, G.E., Williams, R.J.J.N., 1986. Learning representations by back-propagating errors. Nature 323, 533–536. https://doi.org/10.1038/323533a0.

Salawitch, R.J., McBride, L.A., 2022. Australian wildfires depleted the ozone layer. Science 378, 829–830. https://doi.org/10.1126/science.add2056.

Sanders, A.F.J., de Haan, J.F., Sneep, M., Apituley, A., Stammes, P., Vieitez, M.O., Tilstra, L.G., Tuinder, O.N.E., Koning, C.E., Veefkind, J.P., 2015. Evaluation of the operational aerosol layer height retrieval algorithm for Sentinel-5 precursor:

application to O$_2$ a band observations from GOME-2A. Atmos. Meas. Tech. 8, 4947–4977. https://doi.org/10.5194/amt-8-4947-2015.

Sanghavi, S., Martonchik, J.V., Landgraf, J., Platt, U., 2012. Retrieval of the optical depth and vertical distribution of particulate scatterers in the atmosphere using O$_2$ A- and B-band SCIAMACHY observations over Kanpur: a case study. Atmos. Meas. Tech. 5, 1099–1119. https://doi.org/10.5194/amt-5-1099-2012.

Shiraiwa, M., Ueda, K., Pozzer, A., Lammel, G., Kampf, C.J., Fushimi, A., Enami, S., Arangio, A.M., Fröhlich-Nowoisky, J., Fujitani, Y., Furuyama, A., Lakey, P.S.J., Lelieveld, J., Lucas, K., Morino, Y., Pöschl, U., Takahama, S., Takami, A., Tong, H., Weber, B., Yoshino, A., Sato, K., 2017. Aerosol health effects from molecular to global scales. Environ. Sci. Technol. 51, 13545–13567. https://doi.org/10.1021/acs.est.7b04417.

Sun, T., Che, H., Qi, B., Wang, Y., Dong, Y., Xia, X., Wang, H., Gui, K., Zheng, Y., Zhao, H., Ma, Q., Du, R., Zhang, X., 2018. Aerosol optical characteristics and their vertical distributions under enhanced haze pollution events: effect of the regional transport of different aerosol types over eastern China. Atmos. Chem. Phys. 18, 2949–2971. https://doi.org/10.5194/acp-18-2949-2018.

Tackett, J.L., Kar, J., Vaughan, M.A., Getzewich, B.J., Kim, M.H., Vernier, J.P., Omar, A.H., Magill, B.E., Pitts, M.C., Winker, D.M., 2023. The CALIPSO version 4.5 stratospheric aerosol subtyping algorithm. Atmos. Meas. Tech. 16, 745–768. https://doi.org/10.5194/amt-16-745-2023.

Vaswani, A., Shazeer, N., Parmar, N., Uszkoreit, J., Jones, L., Gomez, A. N., Kaiser., Polosukhin, L., 2017. Attention is all you need. Paper presented at the Proceedings of the 31st International Conference on Neural Information Processing Systems, Long Beach, California, USA. 6000 -6010.

Vinjamuri, K.S., Mhawish, A., Banerjee, T., Sorek-Hamer, M., Broday, D.M., Mall, R.K., Latif, M.T., 2020. Vertical distribution of smoke aerosols over upper Indo-Gangetic Plain. Environ. Pollut. 257, 113377. https://doi.org/10.1016/j.envpol.2019.113377.

Wang, S.-H., Lei, H.-W., Pani, S.K., Huang, H.-Y., Lin, N.-H., Welton, E.J., Chang, S.-C., Wang, Y.-C., 2020. Determination of lidar ratio for major aerosol types over western north pacific based on long-term MPLNET data. Remote Sens. 12, 2769. https://doi.org/10.3390/rs12172769.

Wang, Y., Ti, R., Liu, Z., Liu, X., Yu, H., Wei, Y., Fan, Y., Wang, Y., Huang, H., Sun, X., 2025. Enhancing aerosol vertical distribution retrieval with combined LSTM and Transformer model from OCO-2 O$_2$ A-band observations. IEEE J. Sel. Top. Appl. Earth Obs. Remote Sens. 18, 9650–9665. https://doi.org/10.1109/JSTARS.2025.3552310.

Wei, J., Li, Z., Cribb, M., Huang, W., Xue, W., Sun, L., Guo, J., Peng, Y., Li, J., Lyapustin, A., Liu, L., Wu, H., Song, Y., 2020. Improved 1 km resolution PM$_{2.5}$ estimates across China using enhanced space–time extremely randomized trees. Atmos. Chem. Phys. 20, 3273–3289. https://doi.org/10.5194/acp-20-3273-2020.

Wei, J., Li, Z., Lyapustin, A., Wang, J., Dubovik, O., Schwartz, J., Sun, L., Li, C., Liu, S., Zhu, T., 2023. First close insight into global daily gapless 1 km PM$_{2.5}$ pollution, variability, and health impact. Nat. Commun. 14, 8349. https://doi.org/10.1038/s41467-023-43862-3.

Wei, J., Wang, Z., Li, Z., Li, Z., Pang, S., Xi, X., Cribb, M., Sun, L., 2024. Global aerosol retrieval over land from Landsat imagery integrating Transformer and Google Earth Engine. Remote Sens. Environ. 315, 114404. https://doi.org/10.1016/j.rse.2024.114404.

Xu, X., Wang, J., Wang, Y., Zeng, J., Torres, O., Reid, J.S., Miller, S.D., Martins, J.V., Remer, L.A., 2019. Detecting layer height of smoke aerosols over vegetated land and water surfaces via oxygen absorption bands: hourly results from EPIC/DSCOVR in deep space. Atmos. Meas. Tech. 12, 3269–3288. https://doi.org/10.5194/amt-12-3269-2019.

Xu, X., Wang, J., Wang, Y., Zeng, J., Torres, O., Yang, Y., Marshak, A., Reid, J., Miller, S., 2017. Passive remote sensing of altitude and optical depth of dust plumes using the oxygen a and B bands: first results from EPIC/DSCOVR at Lagrange-1 point. Geophys. Res. Lett. 44, 7544–7554. https://doi.org/10.1002/2017GL073939.

Yu, H., Chin, M., Winker, D.M., Omar, A.H., Liu, Z., Kittaka, C., Diehl, T., 2010. Global view of aerosol vertical distributions from CALIPSO lidar measurements and GOCART simulations: Regional and seasonal variations. J. Geophys. Res. Atmos. 115, D00H30. https://doi.org/10.1029/2009JD013364.